Global-Local HROM for non-linear thermal problems with irreversible changes of material states

Alejandro Cosimo[1], Alberto Cardona[1] and Sergio Idelsohn[1,2]

[1]Centro de Investigación de Métodos Computacionales (CIMEC), Santa Fe, Argentina

[2]International Center for Numerical Methods in Engineering (CIMNE) and Institució Catalana de Recerca i Estudis Avançats (ICREA), Barcelona, Spain

Abstract

Problems characterised by highly concentrated moving non-linearities are within the most challenging to be solved by a numerical scheme. The simulation of the Selective Laser Melting Additive Manufacturing process, intractable by traditional numerical techniques, is a problem of this kind. In this work, a *material* Global-Local scheme is proposed for the case of non-linear thermal problems with irreversible phase changes and highly concentrated heat sources. The Global-Local scheme consists in describing the neighbourhood of the heat source by a moving local domain while the material phase fractions are represented in a global domain. A first approach is proposed, in which the equations governing the non-linear thermal problem are assumed to be defined on the local domain only. This is equivalent to consider that the extent of the local domain is large enough to capture the most important variations of the temperature field. Additionally, a Hyper-Reduced Order Model based on a variant of the Energy-Conserving Sampling and Weighting method is proposed for the local domain problem. The performance of the introduced numerical techniques is studied by solving a SLM problem taken from the literature.

Keywords: material Global-Local model, ECSW, HROM, Selective Laser Melting, irreversible phase changes

1 Introduction

Problems characterised by highly concentrated moving non-linearities are within the most challenging to be solved by a numerical scheme. Problems of this kind are frequently found in engineering, making necessary to develop new alternatives to make them tractable from the numerical point of view. One of these problems is the simulation of the Selective Laser Melting (SLM) Additive Manufacturing (AM) process. This process is used to build complex geometries by depositing successive powder beds which are melted with a laser heat source, resulting in the consolidation of the material. The involved phase change problem is extremely non-linear, not only because of the phase changes taking place but also because the powder and the consolidated material properties differ considerably. Another complication for its simulation is the fact that the involved scales are of widely different orders of magnitude and the velocity of

the heat source is quite large. This makes necessary to use very fine meshes and small time increments, and therefore detailed 3D simulations of the process are almost impossible.

We address the simulation of SLM manufacturing where a thermo-mechanical simulation of the process is usually required. Only the non-linear thermal phase change problem will be analysed, however, in a first approach. Different numerical schemes can be found in the literature for dealing with solid/liquid phase change problems, mainly moving mesh or front tracking methods and fixed mesh methods [1]. In this work, the temperature based fixed mesh method proposed by Fachinotti *et al.* [2] is adopted. An important detail in SLM thermal problems is how the laser heat source is modelled. The Goldak heat source [3] is one of the most general and flexible models for welding problems. However, a heat source model specifically developed by Gusarov *et al.* [4, 5] for SLM is available, which was derived based on the laser radiation transfer in a powder layer and will be used in this work. Despite the fact that no metallurgical transformations will be considered, the irreversible transformation from powder to consolidated material needs to be taken into account. An appropriate model handling this transformation is also introduced.

Cosimo *et al.* [6] proposed a Global-Local scheme in order to deal with problems with concentrated moving sources. It consists in describing the neighbourhood of the heat source by a moving local domain with a fine mesh and in describing the global domain by a coarse mesh, with both domains coupled by Lagrange multipliers. Only linear problems were studied in that work, and a Reduced Order Model (ROM) was developed for the local domain. In this work we extend that work to problems with non-linearities coming from material phase changes, mainly to deal with the material phase evolution from powder to consolidated material. A second objective is to develop a Hyper-Reduced Order Model (HROM) for solving the local domain subproblem. We assume that *the extent of the local domain is large enough to capture the most important variations of the temperature field*. This assumption allows us to consider the temperature evolution in the local moving domain uncoupled from the global domain, being the latter used only to track the irreversible change from powder to consolidated material.

The HROM to be used is an *a posteriori* ROM technique based on the Proper Orthogonal Decomposition, in which the solution to a set of training problems is first required. A first reduction is performed to reduce the dimensionality of the test and trial spaces. However, in order to successfully reduce the complexity of non-linear problems, a second reduction must be applied for decreasing the cost of assembling the non-linear forces and the tangent matrix [7, 8]. One option is the Discrete Empirical Interpolation Method (DEIM) [9, 10]. However, in highly non-linear processes such as welding applications, DEIM-based approaches can show an unexpected behaviour, e.g. divergence for an increasing number of sampling entities, making it necessary to consider another options. The Empirical Cubature Method (ECM) proposed by Hernández *et al.* [11] and extended in [12] to multiscale problems, displays better results than DEIM-based approaches. The ECM method shares some common points with the work of An *et al.* [13] and consists in developing a cubature which approximates the involved integrals with a reduced number of integration points. A similar alternative is the Energy-Conserving Sampling and Weighting (ECSW) method proposed by Farhat *et al.* [14, 15], which consists in approximating the assembling of reduced forces by sampling the FEM mesh in a reduced set of elements, and weighting the elements contributions by appropriate *non-negative* factors. In this work, the ECSW method is adopted because it is better adapted to solve phase change problems [2]. However, a modification is proposed in order to reduce the cost of solving an unrestricted least square problem that is involved in the formulation of the ECSW method. Besides, this modification allows to apply the ECSW to self-equilibrated problems.

The paper is organised as follows. In Section 2, a Global-Local model for the solution

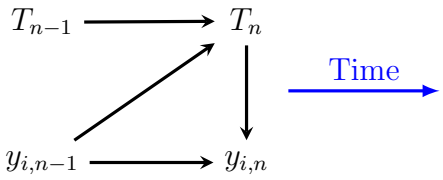

Figure 1: Staggered approach for the coupling of the temperature field and the phase fractions.

of non-linear thermal solid/liquid phase change problems with irreversible material changes is proposed. The formulation of a Hyper-Reduced Order Model for the thermal problem to be solved in the moving local domain is studied in Section 3. The numerical performance of these methods is assessed in Section 4 by solving a SLM problem, which is compared to results of the literature. The conclusions and future work are outlined In Section 5.

2 Material Global-Local model

A *material* Global-Local model for the solution of non-linear phase change problems with highly concentrated moving heat sources is next introduced. Cosimo *et al.* [6] proposed a Global-Local scheme for the solution of problems with moving heat sources. However, non-linearities were not taken into account. In this work we extend the Global-Local model to the analysis of non-linear problems with irreversible material phase changes. For example, the SLM process is characterised by irreversible phase changes which occur when the laser heat source melts the material in powder state resulting in its consolidation. The phase fractions in this process are the powder and the consolidated phase fractions, y_p and y_c, which take values in the range $[0, 1]$ and satisfy $y_p + y_c = 1$. It should be noted that the liquid phase fraction is not explicitly considered in the modelling of this irreversible transformation and will be taken into account in the formulation of the solid/liquid phase change thermal problem.

In order to deal with this problem, a material Global-Local model is proposed. By making the hypothesis that the most important variations of the temperature field are concentrated in the vicinity of the moving laser heat source, it is acceptable to describe the temperature field and the equations governing its evolution only on the support of a local moving domain which follows the heat source. The involved material properties depend on the temperature field and on the material phases at a given point. A linear mixture rule is adopted for the material properties, that is a generic material property m is interpolated as

$$m = m_p y_p + m_c y_c, \tag{1}$$

where m_p and m_c are the properties values of the powder and of the consolidated phases. The local moving domain cannot track the material phase fractions y_p and y_c. For the purpose of tracking the evolution of those phase fractions and modelling the involved kinetics, a global *fixed* domain is introduced.

Two additional issues must be considered under this scenario. On one hand, the procedure of coupling the temperature field and the phase fractions must be specified, and, on the other hand, the communication between the global and the local domains must be specified. The latter issue is required because phase fractions are computed and tracked at the global domain, whilst the temperature field is computed on the local domain. Therefore, the temperature field must be communicated from the local to the global domain and the phase fractions must be communicated from the global to the local domain.

A staggered approach is adopted to couple the temperature field and the phase fractions, (see Fig. 1 and [16] for details). Phase fractions at the previous time step t_{n-1} are used for computing the temperature field at time t_n. The temperature field at time t_n is used as state for computing the phase fractions at the current time t_n. At the beginning of each time step, the global domain transfers the state of the underlying material to the local domain. Meanwhile, at the end of the time step, the temperature field is transferred from the local to the global domain. More specifically, consider the case in which the current time is t_n, then the involved steps are:

1. Move the local domain to the configuration at time t_n.
2. Project the material state, i.e. the phase fractions, from the global domain at time t_{n-1} to the local domain.
3. Compute the temperature field T_n at the current time by solving a set of advective-diffusive equations in the local domain. This problem involves only the degrees of freedom of the local domain.
4. Project the computed temperature field T_n from the local to the global domain.
5. Compute the material phase fractions at the current time $y_{p,n}$ and $y_{c,n}$ on the global domain, using the kinetics modelling the (irreversible) consolidation of the powder state.

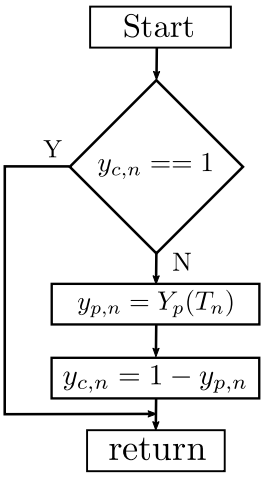

Figure 2: Flowchart with the kinetics modelling the irreversible transformation from powder to consolidated phase.

The kinetics of the irreversible powder consolidation is specified next. The consolidation of the material in powder state takes place at the consolidation temperature T_c in which the material suddenly changes from powder to consolidated. A smoother transition zone from powder to consolidated can also be considered. This is specified by an *equilibrium phase fraction* for the powder phase, denoted by Y_p and used in the simulations as:

$$Y_p(T) = \begin{cases} 1, & T < T_c - T_{sb} \\ 1 - \dfrac{T - (T_c - T_{sb})}{2T_{sb}}, & T_c - T_{sb} \leq T \leq T_c + T_{sb} \\ 0, & T > T_c + T_{sb} \end{cases}, \tag{2}$$

where T_{sb} is a numerical parameter that specifies the temperature semibandwidth of the transition zone from powder to consolidated state. It should observed that taking large values of this parameter will lead to approximate solutions with large transition zones, resulting in a

deviation from the physics of the phenomenon. As a reference, this value was considered to be of the same order than the extent of the mushy zone.

Additionally, irreversibility must be properly handled. That is, the material which is already in consolidated state cannot transform back to powder. The kinetics used to model the introduced irreversible transformation is clearly stated in the form of a flowchart in Fig. 2. Material phase fractions are considered constant by elements and are implemented as internal variables located at the barycentre of the tetrahedral elements of both the global and local domains.

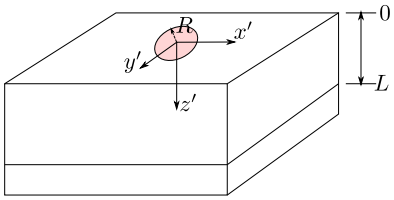

Figure 3: Heat source local coordinate system.

The local domain moves following the heat source. Therefore, the thermal problem at the local domain is governed by an advection-diffusion equation, whose variational formulation is briefly introduced next, see [9] for details. In what follows, let us assume that only Robin and Neumann boundary conditions are specified on the boundaries Γ_c and Γ_q respectively as $k\nabla T \cdot \boldsymbol{n} = h_f(T_f - T)$ and $k\nabla T \cdot \boldsymbol{n} = q_w$, with $\boldsymbol{n}$ being the outward normal to the boundary under consideration, h_f the heat convection coefficient, T_f the external fluid temperature, and q_w a prescribed heat flux. Then, the variational formulation of the problem reads:

Find $T \in \mathcal{H}^1(\Omega)$ *such that* $\forall w \in \mathcal{H}^1(\Omega)$

$$\int_\Omega w \left[\rho c \frac{\partial T}{\partial t} + \rho c \boldsymbol{v} \cdot \nabla T + \rho \mathcal{L} \frac{\partial f_l}{\partial t} - Q\right] \, d\Omega + \int_\Omega \nabla w \cdot \left[k\nabla T - \rho \mathcal{L} f_l \boldsymbol{v}\right] \, d\Omega$$
$$+ \int_{\Gamma_c} w h_f (T - T_f) \, d\Gamma + \int_{\Gamma_q} w q_w \, d\Gamma = 0 \, , \tag{3}$$

where ρ, c, k, $\mathcal{L}$, f_l and $\boldsymbol{v}$ are, respectively, the density, the heat capacity, the conductivity, the latent heat, the liquid phase fraction and the velocity of the heat source. In the case of non-isothermal phase change, the liquid fraction can be described in terms of a linear function of temperature with solidus temperature T_{sol} and liquidus temperature T_{liq} as parameters and given by

$$f_l(T) = \begin{cases} 1 & \text{if } \; T > T_{liq} \\ \dfrac{T - T_{sol}}{T_{liq} - T_{sol}} & \text{if } \; T_{sol} \leq T \leq T_{liq} \\ 0 & \text{if } \; T < T_{sol} \end{cases} . \tag{4}$$

The expression of the heat source Q depends on the application case. The Goldak heat source [3] is one of the most general and flexible for welding problems. However, in the case of SLM, a heat source model specifically developed by Gusarov *et al.* [4] and based on the laser radiation transfer in a powder layer, is available [5, 4]. The parameters used to describe it are the hemispherical reflectivity ρ_h, the extinction coefficient β_h, the effective power W_e considered to be $\frac{2}{3}$ of the nominal laser power W, the powder layer thickness L and the radius of the laser R. The expression of the heat source $Q(x', y', z')$ in the local coordinate system (x', y', z'), see

Fig. 3, is given by

$$Q(x', y', z') = -\beta_h Q_0 \frac{\partial q}{\partial \xi}, \tag{5}$$

where

$$Q_0 = \frac{3W_e}{\pi R^2}\left(1 - \frac{r}{R}\right)^2\left(1 + \frac{r}{R}\right)^2,$$

with $r^2 = x'^2 + y'^2$. The function q has the expression

$$\begin{aligned} q = \frac{\rho_h a}{D(4\rho_h - 3)}\Big(& \left[1 - \rho_h^2\right] e^{-\lambda}\left[(1-a)e^{-2a\xi} + (1+a)e^{2a\xi}\right] \\ & - \left[3 + \rho_h e^{-2\lambda}\right]\left[(1 + a - \rho_h(1-a))e^{2a(\lambda-\xi)} + (1 - a - \rho_h(1+a))e^{2a(\xi-\lambda)}\right]\Big) \\ & - \frac{3(a-\rho_h)\left(e^{-\xi} - \rho_h e^{\xi - 2\lambda}\right)}{4\rho_h - 3}, \end{aligned}$$

where $\xi = \beta_h z'$, $a = \sqrt{1-\rho_h}$, $\lambda = \beta_h L$, and

$$D = (1-a)\left(1 - a - \rho_h\left(1+a\right)\right)e^{-2a\lambda} - (1+a)\left(1 + a - \rho_h\left(1-a\right)\right)e^{2a\lambda}.$$

Let us build a finite element approximation $T^h \in \mathcal{V}^h \subset \mathcal{H}^1$ such that

$$T^h(\boldsymbol{x}, t_n) = \boldsymbol{N}^T \boldsymbol{T}_n, \tag{6}$$

where $\boldsymbol{N}$ denotes the finite element basis and $\boldsymbol{T}_n \in \mathbb{R}^N$ are the FEM (Finite Element Method) nodal degrees of freedom, with N the dimension of the FEM space. Linear tetrahedral elements are used for both the local and global domains. By using a Backward-Euler scheme for time integration, the discrete form of the nonlinear thermal problem to be solved in the local domain reads

$$\boldsymbol{\Pi} = \boldsymbol{G}_n^c + \boldsymbol{G}_n^k + \boldsymbol{G}_n^{vc} + \frac{\boldsymbol{G}_n^l - \boldsymbol{G}_{n-1}^l}{\Delta t} - \boldsymbol{G}_n^{vl} + \boldsymbol{F}_n - \boldsymbol{Q}_n = \boldsymbol{0}, \tag{7}$$

where

$$\boldsymbol{G}_n^c = \int_\Omega \rho c_n \boldsymbol{N}\boldsymbol{N}^T \, d\Omega \, \frac{\boldsymbol{T}_n - \boldsymbol{T}_{n-1}}{\Delta t}, \tag{8}$$

$$\boldsymbol{G}_n^k = \Big(\int_\Omega \nabla \boldsymbol{N} k_n \nabla \boldsymbol{N}^T \Omega + \int_{\Gamma_c} h_{f_n} \boldsymbol{N}\boldsymbol{N}^T \, d\Gamma\Big)\, \boldsymbol{T}_n, \tag{9}$$

$$\boldsymbol{G}_n^{vc} = \int_\Omega \rho c_n \boldsymbol{N}\boldsymbol{v}_n \cdot \nabla \boldsymbol{N}^T \, d\Omega \, \boldsymbol{T}_n, \tag{10}$$

$$\boldsymbol{G}_n^l = \int_\Omega \rho \mathcal{L} \boldsymbol{N} f_{l(n)} \, d\Omega, \tag{11}$$

$$\boldsymbol{G}_n^{vl} = \int_\Omega \rho \mathcal{L} \nabla \boldsymbol{N} \cdot \boldsymbol{v}_n f_{l(n)} \, d\Omega, \tag{12}$$

$$\boldsymbol{F}_n = \int_{\Gamma_q} \boldsymbol{N} q_{w_n} \, d\Gamma - \int_{\Gamma_c} h_{f_n} \boldsymbol{N} T_{f_n} \, d\Gamma, \tag{13}$$

$$\boldsymbol{Q}_n = \int_\Omega \boldsymbol{N} Q_n \, d\Omega. \tag{14}$$

Remark: the local domain is supposed to be coupled to the global domain only through the kinetics of the powder and consolidated phases. The temperature field on the global domain

is not modelled. Introducing the thermal coupling between local and global domains for 3D non-linear problems is left as future work.

A detail of the proposed material Global-Local scheme concerns the projection from the local to the global domain, and vice-versa. This projection is performed by collocation [17] in order to minimise the computational cost. A sufficiently fine mesh is used for the global domain in order to keep low the errors introduced by the projections. The adopted criterion is to make this mesh at least as fine as the one used for the local domain.

Another aspect to consider in the non-linear thermal at the local domain, is the fact that the Péclet numbers will be quite high for SLM applications because the powder conductivity is low and the heat source velocity high. The development of a stabilisation scheme for tackling this problem is considered out of the scope of this work. As it will be observed in the Application Examples, this instability problem will be solved by artificially incrementing the powder conductivity in conflicting zones of the domain.

3 Hyper-Reduced Order Model for the non-linear thermal problem

The hyper-reduction of the non-linear thermal problem in the local domain is analysed next. Despite the fact that the computational cost decreases with the material Global-Local model, the size of the problem to be solved in the local moving domain could be still quite large. Therefore, the formulation of a HROM is of interest to obtain greater acceleration factors.

The proposed HROM is an *a posteriori* ROM technique based on the Proper Orthogonal Decomposition (POD). POD-based ROMs are *a posteriori* techniques, because the construction of the ROM requires first to compute the High-Fidelity (HF) solution to a set of training problems [18]. Generally, two reduction steps are needed for a ROM to be successful for reducing the computation time. In the first reduction, the dimension of the discrete versions of the test and trial spaces is tackled. Nevertheless, for non-linear problems, the cost of assembling the non-linear forces and the tangent matrix can be significant, making necessary to perform a second reduction known as hyper-reduction [19, 11].

A reduced basis for the test and trial spaces is built in the first reduction step. For this purpose, a set of *snapshots* of the solution to training problems is collected [20]. Then, the Singular Value Decomposition [21] of the snapshots matrix is computed, taking the first n_p left singular vectors $\boldsymbol{\Psi}$ (also referred to as *POD modes*) as a reduced basis to capture the response of the system under study. In order for the ROM to be successful, n_p must be much smaller than the number of DOFs N of the HF model, that is $n_p \ll N$. Previous experiences had shown that this property is satisfied for welding problems [9, 6] provided the frame of reference moves attached to the heat source, and a similar strategy is used in this case. We assumed for simplicity that no essential boundary conditions are present; if this is not the case, we refer to [22] for details on how to proceed.

In what follows, we specifically analyse the reduction of the non-linear conductivity term denoted for simplicity by $\boldsymbol{G}$, that is $\boldsymbol{G} \equiv \boldsymbol{G}_n^k$ and re-written here for clarity as:

$$\boldsymbol{G} = \int_\Omega \nabla \boldsymbol{N} k_n \nabla \boldsymbol{N}^T \boldsymbol{T}_n \, d\Omega = \sum_{e \in E} \boldsymbol{L}_e^T \bar{\boldsymbol{g}}_e \, , \tag{15}$$

where E is the set of Finite Elements (FEs), $\boldsymbol{L}_e$ is the assembling operator, and $\bar{\boldsymbol{g}}_e$ is the contribution to the integral corresponding to element e. After the first reduction step, the

following reduced-form of the conductivity term is obtained:

$$\tilde{\boldsymbol{G}} = \sum_{e \in E} \boldsymbol{\Psi}^T \boldsymbol{L}_e^T \bar{\boldsymbol{g}}_e = \sum_{e \in E} \boldsymbol{\Psi}_e^T \bar{\boldsymbol{g}}_e = \sum_{e \in E} \boldsymbol{g}_e, \tag{16}$$

where $\boldsymbol{\Psi}_e$ is the restriction of the rows of $\boldsymbol{\Psi}$ to the global DOFs indexed by element e.

The second reduction step is next described. It consists in tackling the cost associated to the assembling of the non-linear forces and the tangent matrix by approximating these quantities by sampling just a few elements or Gauss points. The Discrete Empirical Interpolation Method (DEIM) can be used for this purpose [9]. However, SLM processes are extremely non-linear and the instability characteristic of DEIM-based approaches makes necessary to consider other options. In this context, the term instability is used to refer to a situation in which the HROM behaves unexpectedly, *e.g.* by diverging as the number of sampling entities is incremented. Hernández *et al.* [11] presented the Empirical Cubature Method which shows a good behaviour from the stability point of view. It is based on the work of An *et al.* [13] and consists in developing a cubature which approximates the involved integrals with a reduced number of integration points. Despite the fact that this method works very well, it requires to modify the FEM code at the element level because the FEM formulation must be able to provide sampled values of the integrand at FE Gauss points. However, the formulation we used for phase change problems [2, 23], is only able to provide *integrated* values at the nodes of each FE. Therefore, another option needs to be considered.

The Energy-Conserving Sampling and Weighting method proposed by Farhat *et al.* [14, 15] is a good alternative. It is based on sampling elements, *i.e.* it can deal from its conception with formulations which are only able to provide *integrated* values at the nodes of each FE, and it has good behaviour from the stability point of view. The ECSW method consists in approximating the assembling of $\tilde{\boldsymbol{G}}$, Eq. (16), by means of sampling the FEM mesh at a reduced set of n_z elements, denoted by $\tilde{E}$, and weighting the elements contributions by appropriate *non-negative* weights w_e. The idea is based on finding weights w_e and a set of elements $\tilde{E}$, such that

$$\tilde{\boldsymbol{G}} = \sum_{e \in E} \boldsymbol{g}_e \approx \sum_{e=1}^{n_z} w_e \boldsymbol{g}_{z_e}, \tag{17}$$

where z_e denotes the mapping from the numbering used for identifying the elements in the reduced set $\tilde{E}$ to the numbering identifying the corresponding element in the FE set E.

In what follows, let n_j be the number of training samples, and denote with $\tilde{G}_i^j$ and $g_{i,e}^j$ the i component of the assembled forces and element contributions for the training sample j. In order to find the weights w_e and the indices z_e, the following errors need to be minimised:

$$r_i^j = \sum_{e=1}^{n_z} w_e g_{i,z_e}^j - \tilde{G}_i^j, \qquad \text{for} \quad i = 1, 2, \cdots, n_p; \;\; j = 1, 2, \cdots, n_j. \tag{18}$$

In matrix notation it takes the form

$$\boldsymbol{J}_z \boldsymbol{w} = \boldsymbol{b} \tag{19}$$

with

$$\boldsymbol{J}_z = \begin{bmatrix} \boldsymbol{g}_{z_1}^1 & \cdots & \boldsymbol{g}_{z_{n_z}}^1 \\ \vdots & \ddots & \vdots \\ \boldsymbol{g}_{z_1}^{n_j} & \cdots & \boldsymbol{g}_{z_{n_z}}^{n_j} \end{bmatrix} \in \mathbb{R}^{n_j n_p \times n_z} \qquad \boldsymbol{w} = \begin{bmatrix} w_1 \\ \vdots \\ w_{n_z} \end{bmatrix} \in \mathbb{R}^{n_z} \qquad \boldsymbol{b} = \begin{bmatrix} \tilde{\boldsymbol{G}}^1 \\ \vdots \\ \tilde{\boldsymbol{G}}^{n_j} \end{bmatrix} \in \mathbb{R}^{n_j n_p} \tag{20}$$

Then, the associated minimisation problem reads

$$(\boldsymbol{w}, \boldsymbol{z}) = \underset{\bar{\boldsymbol{w}} \geq 0, \bar{\boldsymbol{z}}}{\arg\min} \, ||\boldsymbol{J}_{\bar{\boldsymbol{z}}} \bar{\boldsymbol{w}} - \boldsymbol{b}||. \tag{21}$$

In order to find the elements $\boldsymbol{z}$ to sample and the corresponding weights $\boldsymbol{w}$, a modified version of the algorithm of Lawson and Hanson [24] for solving Non-Negative Least Square (NNLS) problems is used. The pseudo-code of this algorithm is given in Algorithm (1).

Algorithm 1 NNLS to find elements and weights

procedure NNLS(J, b, τ, n_z)
  $z \leftarrow \emptyset$ ▷ variable storing elements to be sampled
  $y \leftarrow \{1, 2, \cdots, n_e\}$
  $n \leftarrow 0$
  $r \leftarrow b$
  while $||r||/||b|| > \tau$ **and** $n \leq n_z$ **do**
    Compute new element i as $i = \arg\max_{j \in y} J_y^T r$ ▷ select the element to sample
    ▷ in a greedy manner
    Move i from set y to set z
    $n \leftarrow n + 1$
    while True **do**
      $\beta = \arg\min_{\eta \in \mathbb{R}^{|z|}} ||J_z \eta - b||_2$ ▷ unrestricted least squares
      if all($\beta \geq 0$) **then**
        $w = \beta$
        break
      end if
      $d \leftarrow \min\left(\frac{w_i}{w_i - \beta_i}\right)$ for $i \in$ with $\beta_i < 0$
      $w \leftarrow w + d\,(\beta - w)$
      $y \leftarrow$ zero_value_indices(w)
      $z \leftarrow \{1, 2, \cdots, n_e\} \setminus y$
      $n \leftarrow |z|$
    end while
    $r \leftarrow b - J_z w$
    $n \leftarrow |z|$
  end while
end procedure

It should be noted that Farhat *et al.* [14, 15] used a slightly different approach to introduce the ECSW method. They end up with an optimisation problem defined in the zero-norm, which is NP-hard to solve. Therefore, they re-stated the problem in the L_2 norm, and proposed to solve inexactly the resulting NNLS problem. They referred to that algorithm as *sparse-NNLS*, which is very similar to the one presented in Algorithm (1).

An important detail concerning the hyper-reduction of phase change problems is how to deal with the many non-linear terms that appear in Eq. (7). In this work, each non-linear term is separately hyper-reduced, leading to a HROM with the following residual:

$$\tilde{\boldsymbol{\Pi}} = \tilde{\boldsymbol{G}}_n^c + \tilde{\boldsymbol{G}}_n^k + \tilde{\boldsymbol{G}}_n^{vc} + \frac{\tilde{\boldsymbol{G}}_n^l - \tilde{\boldsymbol{G}}_{n-1}^l}{\Delta t} - \tilde{\boldsymbol{G}}_n^{vl} + \boldsymbol{\Psi}^T \boldsymbol{F}_n - \boldsymbol{\Psi}^T \boldsymbol{Q}_n = \boldsymbol{0}. \tag{22}$$

In this expression, the terms with tilde are the ones to be hyper-reduced with the ECSW method. It should be noted that the terms $\boldsymbol{F}_n$ and $\boldsymbol{Q}_n$ are not hyper-reduced. On one hand the

term $\boldsymbol{F}_n$ is not hyper-reduced because in the examples to be solved this term does not contribute. However, if this term contributes to the problem *and* its contribution is time dependent, it can be hyper-reduced by considering it part of the conductivity term $\boldsymbol{G}_n^k$ and hyper-reduce both as a single entity. On the other hand, the heat source term $\boldsymbol{Q}_n$ is not hyper-reduced because the local domain moves following the heat source, therefore its contribution can be computed only once at the beginning of the simulation.

3.1 Reformulation of the ECSW method

Note that an unrestricted least squares problem must be solved at each iteration of Algorithm (1). The cost of solving it increases considerably with the size of the matrix $\boldsymbol{J}_z$. Therefore, we reformulate the ECSW method to reduce the size of this matrix using an approach similar to that presented by Hernández *et al.* in the context of the ECM method [11]. From Eq. (17), the assembling of the component i of $\tilde{\boldsymbol{G}}^j$ for the training sample j can be written as

$$\tilde{G}_i^j = \sum_{e \in E} g_{i,e}^j = \sum_{e \in E} 1 \cdot g_{i,e}^j = \mathbf{1}^T \boldsymbol{\mathcal{G}}_{\mathrm{i}}^{\mathrm{j}}, \tag{23}$$

where $\mathbf{1} = [1, 1, \cdots 1]^T$ and $\boldsymbol{\mathcal{G}}_{\mathrm{i}}^{\mathrm{j}} = [g_{i,1}^j, g_{i,2}^j, \cdots, g_{i,n_e}^j]^T$. Then, $\mathbf{1}^T$ can be interpreted as a linear transformation $\boldsymbol{\mathcal{T}} = \mathbf{1}^T$ which maps elements from $\mathbb{R}^{n_e}$ to $\mathbb{R}$. Therefore, the domain of the linear transformation $\boldsymbol{\mathcal{T}}$ can be decomposed into two orthogonal components, namely the Null space of $\boldsymbol{\mathcal{T}}$, $\mathcal{N}(\boldsymbol{\mathcal{T}})$, and the range space of $\boldsymbol{\mathcal{T}}^T$, $\mathcal{R}(\boldsymbol{\mathcal{T}}^T)$, *i.e.* $\mathbb{R}^{n_e} = \mathcal{N}(\boldsymbol{\mathcal{T}}) \oplus \mathcal{R}(\boldsymbol{\mathcal{T}}^T)$. By noting that $\mathbf{1}$ spans $\mathcal{R}(\boldsymbol{\mathcal{T}}^T)$, the projection $\mathring{\boldsymbol{\mathcal{G}}}_{\mathrm{i}}^{\mathrm{j}}$ of $\boldsymbol{\mathcal{G}}_{\mathrm{i}}^{\mathrm{j}}$ on $\mathcal{R}(\boldsymbol{\mathcal{T}}^T)$ is given by

$$\mathring{\boldsymbol{\mathcal{G}}}_{\mathrm{i}}^{\mathrm{j}} = \frac{\mathbf{1}}{||\mathbf{1}||} \left(\frac{\mathbf{1}^T}{||\mathbf{1}||} \boldsymbol{\mathcal{G}}_{\mathrm{i}}^{\mathrm{j}} \right) = \mathbf{1} \frac{\tilde{G}_i^j}{n_e} = \frac{1}{n_e} \begin{bmatrix} \tilde{G}_i^j \\ \vdots \\ \tilde{G}_i^j \end{bmatrix}. \tag{24}$$

The projection of $\boldsymbol{\mathcal{G}}_{\mathrm{i}}^{\mathrm{j}}$ on $\mathcal{N}(\boldsymbol{\mathcal{T}})$, denoted by $\hat{\boldsymbol{\mathcal{G}}}_{\mathrm{i}}^{\mathrm{j}}$, is computed by subtracting $\mathring{\boldsymbol{\mathcal{G}}}_{\mathrm{i}}^{\mathrm{j}}$ from $\boldsymbol{\mathcal{G}}_{\mathrm{i}}^{\mathrm{j}}$, that is

$$\hat{\boldsymbol{\mathcal{G}}}_{\mathrm{i}}^{\mathrm{j}} = \boldsymbol{\mathcal{G}}_{\mathrm{i}}^{\mathrm{j}} - \mathring{\boldsymbol{\mathcal{G}}}_{\mathrm{i}}^{\mathrm{j}} = \begin{bmatrix} g_{i,1}^j - \dfrac{\tilde{G}_i^j}{n_e} \\ \vdots \\ g_{i,n_e}^j - \dfrac{\tilde{G}_i^j}{n_e} \end{bmatrix} = \begin{bmatrix} \hat{g}_{i,1}^j \\ \vdots \\ \hat{g}_{i,n_e}^j \end{bmatrix}, \tag{25}$$

which provides the following equation:

$$0 = \mathbf{1}^T \hat{\boldsymbol{\mathcal{G}}}_{\mathrm{i}}^{\mathrm{j}}. \tag{26}$$

The reduced set of weights $\boldsymbol{w}$ and elements $\tilde{E}$ is then determined such that the following quantities are well approximated

$$0 = \mathbf{1}^T \hat{\boldsymbol{\mathcal{G}}}_{\mathrm{i}}^{\mathrm{j}} \approx \sum_{e=1}^{n_z} w_e \hat{g}_{i,z_e}^j, \qquad \text{for} \quad i = 1, 2, \cdots, n_p; \;\; j = 1, 2, \cdots, n_j; \tag{27}$$

$$n_e = \mathbf{1}^T \mathbf{1} \approx \sum_{e=1}^{n_z} w_e. \tag{28}$$

Then, we have to solve a NNLS problem similar to that given by Eq. (21), but with $\boldsymbol{J}_z$ and $\boldsymbol{b}$ redefined as:

$$\boldsymbol{J}_z = \begin{bmatrix} \hat{\boldsymbol{g}}^1_{z_1} & \cdots & \hat{\boldsymbol{g}}^1_{z_{n_z}} \\ \vdots & \ddots & \vdots \\ \hat{\boldsymbol{g}}^{n_j}_{z_1} & \cdots & \hat{\boldsymbol{g}}^{n_j}_{z_{n_z}} \\ 1 & \cdots & 1 \end{bmatrix} \in \mathbb{R}^{(n_j n_p+1)\times n_z}, \qquad \boldsymbol{b} = \begin{bmatrix} 0 \\ \vdots \\ 0 \\ n_e \end{bmatrix} \in \mathbb{R}^{(n_j n_p+1)}. \tag{29}$$

An additional improvement can be done. Suppose that we know in advance a basis $\boldsymbol{\Phi}_s$, with $s = 1, 2, \cdots, n_s$, which spans the space of $\hat{\boldsymbol{\mathcal{G}}}^{\mathrm{j}}_{\mathrm{i}}$. Then, $\hat{\boldsymbol{\mathcal{G}}}^{\mathrm{j}}_{\mathrm{i}} = \sum_{s=1}^{n_s} \boldsymbol{\Phi}_s c_s$ and Eq. (27) can be equivalently written as

$$0 \approx \sum_{e=1}^{n_z} w_e \hat{g}^j_{i,z_e} = \sum_{e=1}^{n_z} w_e \sum_{s=1}^{n_s} \Phi_{s,z_e} c_s = \sum_{s=1}^{n_s} \left(\sum_{e=1}^{n_z} w_e \Phi_{s,z_e} \right) c_s, \tag{30}$$

where $\Phi_{s,e}$ is the e component of basis vector $\boldsymbol{\Phi}_s$. Due to the fact that parameters c_s are arbitrary, the previous expression is equivalent to

$$0 \approx \sum_{e=1}^{n_z} w_e \Phi_{s,z_e}, \qquad \text{for } \; s = 1, 2, \cdots, n_s. \tag{31}$$

Adopting this formulation the expression for $\boldsymbol{J}_z$ and $\boldsymbol{b}$ are given by

$$\boldsymbol{J}_z = \begin{bmatrix} \Phi_{1,z_1} & \cdots & \Phi_{1,z_{n_z}} \\ \vdots & \ddots & \vdots \\ \Phi_{n_s,z_1} & \cdots & \Phi_{n_s,z_{n_z}} \\ 1 & \cdots & 1 \end{bmatrix} \in \mathbb{R}^{(n_s+1)\times n_z}, \qquad \boldsymbol{b} = \begin{bmatrix} 0 \\ \vdots \\ 0 \\ n_e \end{bmatrix} \in \mathbb{R}^{(n_s+1)}. \tag{32}$$

The basis $\boldsymbol{\Phi}$ is built by collecting snapshots of $\hat{\boldsymbol{g}}^j_e$ at each FE, arranged as

$$\hat{\boldsymbol{\mathcal{H}}} = [\hat{\boldsymbol{\mathcal{G}}}^1 \ldots \hat{\boldsymbol{\mathcal{G}}}^j \ldots \hat{\boldsymbol{\mathcal{G}}}^{n_j}] \tag{33}$$

Then, the Singular Value Decomposition (SVD) of $\hat{\boldsymbol{\mathcal{H}}}$ is computed and the most n_s significant left singular vectors are taken as the basis $\boldsymbol{\Phi}$.

In order to solve for $\boldsymbol{w}$ and gather the reduced set of elements $\tilde{E}$, an algorithm similar to the one presented in Algorithm (1) is adopted. The number of POD modes n_s used for the basis $\boldsymbol{\Phi}$ is always taken as $n_s = n_z - 1 = |\tilde{E}| - 1$. In this way, the NNLS solver will always converge to a solution with an error close to machine precision.

Remark: from Eq. (20) it can be noted that self-equilibrated problems result in an ill-posed minimisation problem. With the modification introduced in this section, the ECSW method can also deal with this kind of problems.

3.2 Alternative reformulation of the ECSW method. Equivalence with the ECM method.

It can be observed from Eq. (32) that an additional restriction is added to avoid ill-posedness in self-equilibrated problems: the weights sum must be equal to the number of elements n_e. In

this sub-section, we scale this restriction so that the weights sum equals the volume V of the domain, to show the equivalence with the ECM method. Let us re-write Eq. (23) as

$$\tilde{G}_i^j = \sum_{e \in E} \sqrt{\Omega_e} \cdot \frac{g_{i,e}^j}{\sqrt{\Omega_e}} = \sqrt{\boldsymbol{\Omega}_e}^T \boldsymbol{\mathcal{V}}_{\mathrm{i}}^{\mathrm{j}}, \tag{34}$$

where $\sqrt{\boldsymbol{\Omega}_e}^T = [\sqrt{\Omega_1}, \sqrt{\Omega_2}, \cdots \sqrt{\Omega_{n_e}}]$ and $\boldsymbol{\mathcal{V}}_{\mathrm{i}}^{\mathrm{j}} = [g_{i,1}^j/\sqrt{\Omega_1}, g_{i,2}^j/\sqrt{\Omega_2}, \cdots, g_{i,n_e}^j/\sqrt{\Omega_{n_e}}]^T$.

It should be observed that in this case, the linear transformation operator is given by $\boldsymbol{\mathcal{T}} = \sqrt{\boldsymbol{\Omega}_e}^T$, from which the projection of $\boldsymbol{\mathcal{V}}_{\mathrm{i}}^{\mathrm{j}}$ to $\mathcal{N}(\boldsymbol{\mathcal{T}})$ is given by

$$\breve{\boldsymbol{\mathcal{V}}}_{\mathrm{i}}^{\mathrm{j}} = \boldsymbol{\mathcal{V}}_{\mathrm{i}}^{\mathrm{j}} - \frac{\sqrt{\boldsymbol{\Omega}_{\mathrm{e}}}}{||\sqrt{\boldsymbol{\Omega}_{\mathrm{e}}}||} \left(\frac{\sqrt{\boldsymbol{\Omega}_{\mathrm{e}}}^T}{||\sqrt{\boldsymbol{\Omega}_{\mathrm{e}}}||} \boldsymbol{\mathcal{V}}_{\mathrm{i}}^{\mathrm{j}} \right) = \begin{bmatrix} \sqrt{\Omega_1} \left(\dfrac{g_{i,1}^j}{\Omega_1} - \dfrac{\tilde{G}_i^j}{V} \right) \\ \vdots \\ \sqrt{\Omega_{n_e}} \left(\dfrac{g_{i,n_e}^j}{\Omega_{n_e}} - \dfrac{\tilde{G}_i^j}{V} \right) \end{bmatrix} = \begin{bmatrix} \breve{g}_{i,1}^j \\ \vdots \\ \breve{g}_{i,n_e}^j \end{bmatrix}, \tag{35}$$

where V is the volume of the analysis domain. Therefore, the reduced set of weights $\boldsymbol{w}$ now must comply to

$$0 = \sqrt{\boldsymbol{\Omega}_{\mathrm{e}}}^T \breve{\boldsymbol{\mathcal{V}}}_{\mathrm{i}}^{\mathrm{j}} \approx \sum_{e=1}^{n_z} \frac{w_e}{\sqrt{\Omega_{z_e}}} \breve{g}_{i,z_e}^j, \quad \text{for } \; i = 1, 2, \cdots, n_p \;\; j = 1, 2, \cdots, n_j \tag{36}$$

$$V = \sqrt{\boldsymbol{\Omega}_{\mathrm{e}}}^T \sqrt{\boldsymbol{\Omega}_{\mathrm{e}}} \approx \sum_{e \in \tilde{E}} w_e. \tag{37}$$

Then, we have to solve a NNLS problem similar to that given by Eq. (21), but with $\boldsymbol{J}_z$ and $\boldsymbol{b}$ redefined as:

$$\boldsymbol{J}_z = \begin{bmatrix} \breve{\boldsymbol{g}}_{z_1}^1 & \cdots & \breve{\boldsymbol{g}}_{z_{n_z}}^1 \\ \vdots & \ddots & \vdots \\ \breve{\boldsymbol{g}}_{z_1}^{n_j} & \cdots & \breve{\boldsymbol{g}}_{z_{n_z}}^{n_j} \\ \sqrt{\Omega_{z_1}} & \cdots & \sqrt{\Omega_{z_{n_z}}} \end{bmatrix}, \in \mathbb{R}^{(n_j n_p + 1) \times n_z}, \qquad \boldsymbol{b} = \begin{bmatrix} 0 \\ \vdots \\ 0 \\ V \end{bmatrix} \in \mathbb{R}^{(n_j n_p + 1)}. \tag{38}$$

As done before, a basis $\boldsymbol{\Phi}$ is built for the space of $\breve{\boldsymbol{\mathcal{V}}}_{\mathrm{i}}^{\mathrm{j}}$ by taking the left singular vectors of the snapshots matrix

$$\hat{\boldsymbol{\mathcal{G}}}^v = [\breve{\boldsymbol{\mathcal{V}}}^1 \ldots \breve{\boldsymbol{\mathcal{V}}}^2 \ldots \breve{\boldsymbol{\mathcal{V}}}^{n_j}]. \tag{39}$$

This results in the following expression for $\boldsymbol{J}_z$ and $\boldsymbol{b}$:

$$\boldsymbol{J}_z = \begin{bmatrix} \Phi_{1,z_1} & \cdots & \Phi_{1,z_{n_z}} \\ \vdots & \ddots & \vdots \\ \Phi_{n_s,z_1} & \cdots & \Phi_{n_s,z_{n_z}} \\ \sqrt{\Omega_{z_1}} & \cdots & \sqrt{\Omega_{z_{n_z}}}. \end{bmatrix} \in \mathbb{R}^{(n_s+1) \times n_z}, \qquad \boldsymbol{b} = \begin{bmatrix} 0 \\ \vdots \\ 0 \\ V \end{bmatrix} \in \mathbb{R}^{(n_s+1)}. \tag{40}$$

Remark: Equivalence between the ECSW and the ECM methods. In case only one Gauss point is used per finite element, the equivalence of both methods follows from Eq. (34). Under this scenario, contributions $g_{i,e}^j$ are computed as $g_{i,e}^j = \Omega_e f_i^j(\bar{\boldsymbol{x}}_e)$, where $\bar{\boldsymbol{x}}_e$ is the

barycentre of the element and f_i^j is the component i of the integrand of Eq. (15) for the training sample j. Therefore,

$$\tilde{G}_i^j = \sum_{e \in E} \Omega_e \frac{g_{i,e}^j}{\Omega_e} = \sum_{e \in E} \Omega_e \frac{\Omega_e f_i^j(\bar{\boldsymbol{x}}_e)}{\Omega_e} = \sum_{e \in E} \Omega_e f_i^j(\bar{\boldsymbol{x}}_e), \tag{41}$$

result on which is based the ECM method. The equivalence is, therefore, demonstrated.

3.3 A note on the computation of the Singular Value Decomposition

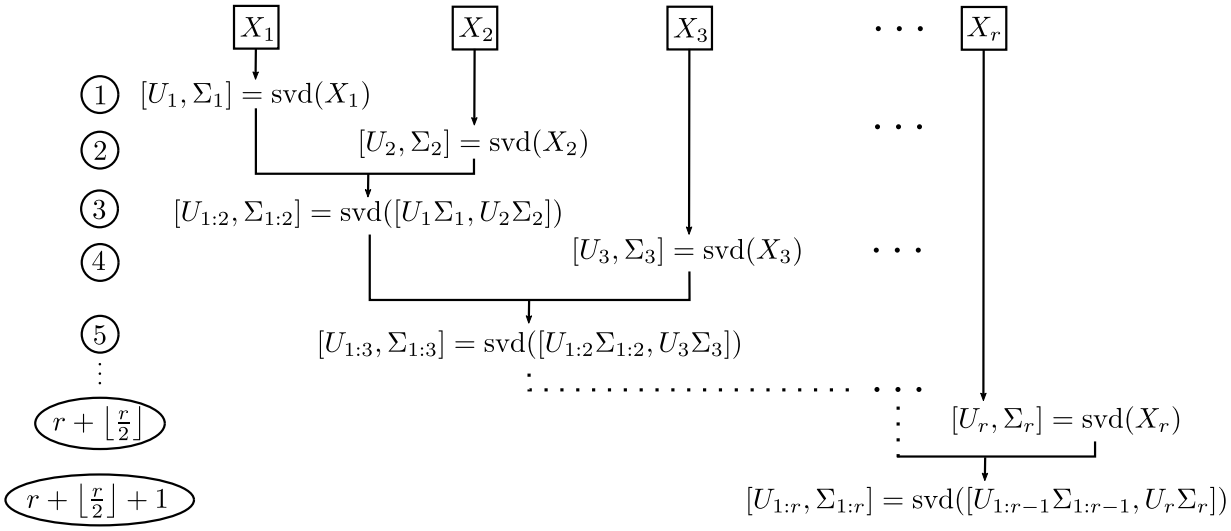

Figure 4: Algorithm for computing the SVD of large snapshots matrices.

Two alternatives of the ECSW method have been proposed. In both of them, the SVD of the snapshots matrix for the reduced generalised forces, generically denoted in what follows by $\boldsymbol{X}$, needs to be computed. It should be observed that this matrix could be quite large in size making it practically impossible to compute its SVD because of memory requirements. One option would be to use domain decomposition and apply parallelisation, a complicated option. One disadvantage of this option is that from a global point-of-view the number of selected elements to be sampled will be larger than to apply the selection algorithm to the global domain. Another option to tackle this issue was proposed by Hernández *et al.* [11] by using a *partitioned* SVD. It is based on approximating the SVD of the snapshots matrix by partitioning it into block matrices and computing the individual SVDs of these block matrices. In brief, suppose that the snapshots matrix $\boldsymbol{X}$ is partitioned into r blocks as $\boldsymbol{X} = [\boldsymbol{X}_1,\ \boldsymbol{X}_2, \cdots, \boldsymbol{X}_r]$ and that the first n left singular vectors need to be computed. Then, the SVD of each block is computed by keeping only the first $r_m = \min(\text{rank}(\boldsymbol{X}_m), n)$ vectors so that $\boldsymbol{X}_m = \boldsymbol{U}_m \boldsymbol{\Sigma}_m \boldsymbol{V}_m^T + \boldsymbol{E}_m$, where $\boldsymbol{E}_m$ is the matrix of errors in taking the SVD of rank r_m. Following, the sought left singular vectors $\boldsymbol{U}$ are obtained from the computation of the SVD of rank n of the matrix $\bar{\boldsymbol{X}} = [\boldsymbol{U}_1\Sigma_1,\ \boldsymbol{U}_2\Sigma_2, \cdots, \boldsymbol{U}_r\Sigma_r]$.

The approach followed in this paper is based on the partitioned SVD. The algorithm is depicted in Fig. 4. It should be noted that it is a sequential algorithm which proceeds in a cascade manner, but controlling the amount of memory needed by each SVD. Another option would be to base the algorithm in a binary tree displaying a high degree of parallelism and allowing to run it in a cluster.

Finally, in order to minimise the time spent on computing the SVD, the randomised-SVD implemented by Voronin and Martinsson [25] is used.

4 Application Examples

Two application examples are shown to assess the performance of the introduced methods. First, the numerical behaviour of the material Global-Local model is studied by solving a SLM manufacturing problem in which one layer of powder is heated by a laser beam. Results for two different velocity values of the heat source are computed and compared to those found in [5, 4]. In the second example, the proposed HROM for the local domain is tested by solving one of the previous problems. The on-line performance of the HROM model is tested by running the same problem used for training, with the purpose of showing that it has good stability properties and approximates correctly the behaviour of the system under study. In the presented examples, the value for T_{sb}, see Eq. (2), is 10K. The tetrahedral elements modelling the phase change are exactly integrated (see Fachinotti *et al.* [2]).

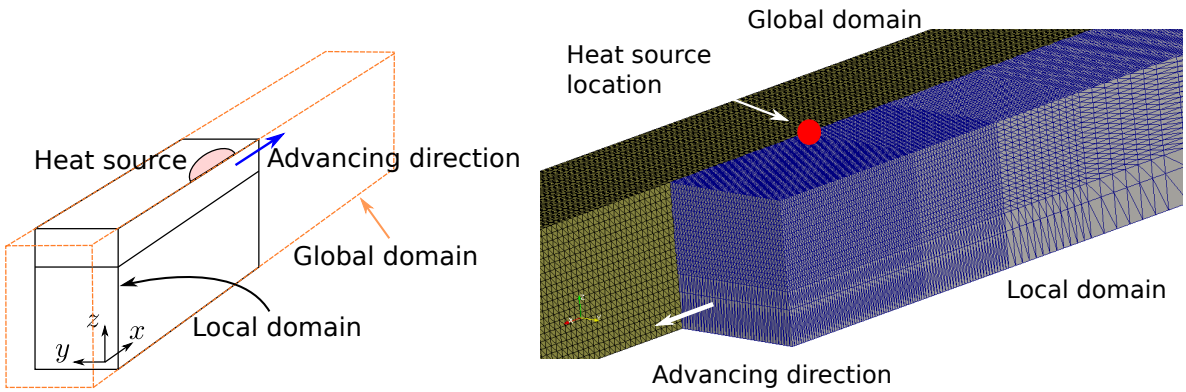

(a) Global and local domains' configurations.

(b) Meshes used for the global and local domains. The local domain has been mirrored for the sake of its visualisation.

Figure 5: Details of the global and local domains meshes. The local domain mesh is refined in the vicinity of the heat source.

4.1 Example 1

In order to verify the numerical performance of the High Fidelity material Global-Local scheme proposed in Section 2, the SLM problem of Gusarov *et al.* [4] and also solved by Hodge *et al.* [5] is studied for two different values of the heat source velocity. The problem consists in the laser beam heating of a block of 0.2 mm depth in which the top 0.05 mm is powder and the rest is consolidated material. The laser moves along the x-direction and, therefore, only one half of the domain is modelled with a symmetry boundary condition at $y = 0$ (Fig. 5a). The global and local domains can be seen in that figure. Dimensions of the local domain are (1.2 mm, 0.2 mm, 0.2 mm), whilst those of the global domain are (2.4 mm, 0.2 mm, 0.2 mm). The meshes are shown in Fig. 5b. The local domain mesh has a total of 576,000 tetrahedra with a refinement in the vicinity of the heat source towards the advancing direction. The powder conductivity is artificially incremented in the front part of the domain, as described in Table 1. These refinement and conductivity increment are done in order to lower the Pèclet number in that area, and stabilise the numerical solution and avoid spurious oscillations. The global domain has a total of 1,152,000 tetrahedra. A non-isothermal phase change model is assumed, with a solidus temperature, $T_{sol} = 1,678$ K and a liquidus temperature, $T_{liq} = 1,718$ K. The Gusarov heat source, Eq. (5), is used for modelling the energy input from the laser. It is

defined by the following parameters: $W_e = 30$ W, $\rho_h = 0.7$, $\beta_h = 60,000\ \frac{1}{\text{m}}$, $R = 0.06$ mm and $\lambda = 3$. The initial temperature is taken to be 303 K and the material properties are given in Table 1. A time increment of 10^{-5} s is used for the time interval $[0, 0.00416\text{ s}]$.

Description	Value
Specific heat, powder	2.98@1,600, 5.95@1,700 (MJ/m^{3}K@K)
Specific heat, consolidated	4.25@1,600, 5.95@1,700 (MJ/m^{3}K@K)
Thermal conductivity, powder	0.2@200, 0.3@1,600, 20@1,700 (W/mK@K)
Thermal conductivity incremented, powder	0.2@200, 3@1,600, 20@1,700 (W/mK@K)
Thermal conductivity, consolidated	20 (W/mK@K)

Table 1: Thermo-physical properties for Examples 1 and 2 [5].

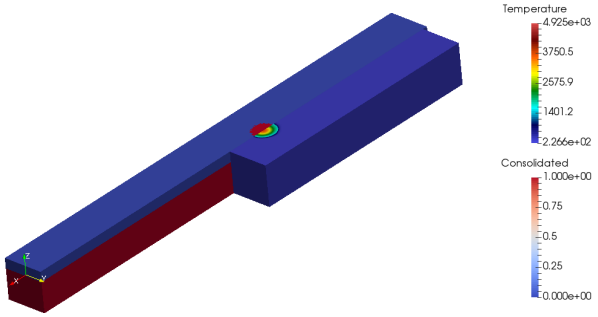

(a) Solution for $v = 120\frac{\text{mm}}{\text{s}}$ at time instant: 0.0002s

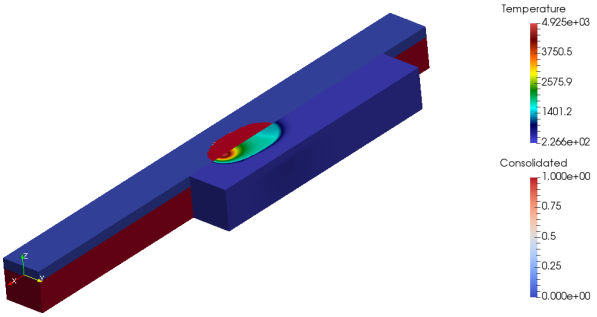

(b) Solution for $v = 120\frac{\text{mm}}{\text{s}}$ at time instant: 0.0022s

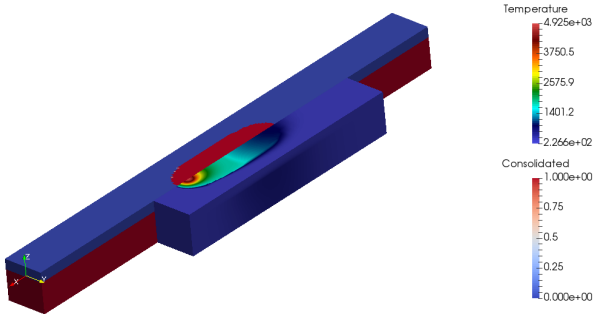

(c) Solution for $v = 120\frac{\text{mm}}{\text{s}}$ at time instant: 0.00416s

Figure 6: Solution to the problem at different time instants for $v = 120\frac{\text{mm}}{\text{s}}$. The evolution of the phase fraction of the consolidated material is shown on the global domain. The temperature field is shown on the local moving domain, which is drawn mirrored for the sake of visualisation.

Two advancement velocities are tested: $v = 120\frac{\text{mm}}{\text{s}}$ and $v = 240\frac{\text{mm}}{\text{s}}$. In Figs. 6a-c, the evolution of the phase fraction of the consolidated material and of the temperature field for a velocity $v = 120\frac{\text{mm}}{\text{s}}$ for the heat source are shown for three time instants. The purpose of these figures is showing how the material Global-Local model works. As it can appreciated, the global domain is fixed and tracks the material phase changes, mainly the irreversible transformation from powder to consolidated material. On the other hand the local domain moves following the laser heat source while coupled to the material state computed on the global domain. The results look good without the presence of spurious oscillations. However, it must be called the attention that the minimum computed temperature is 226.6K which is below the initial

temperature of 303K. A much finer mesh or a good stabilisation scheme would be needed in order to make the minimum computed temperature closer to 303K. Despite this fact, from a general point-of-view the obtained solution is of good quality.

In order to validate the proposed material Global-Local model, the results for both velocities are compared to those obtained by Gusarov *et al.* [4] and by Hodge *et al.* [5]. More specifically, the shape and the maximum depth of the melt pool are taken as sources of comparison. The melt pool is considered to be defined by the temperature contour at 1700K. In Figs. 7 and 8 the comparison of the obtained results for the melt pool depth and its shape can be respectively observed. From these figures, it can be concluded that the proposed material Global-Local model performs well from the numerical point-of-view, showing results similar to those obtained by state-of-the-art numerical techniques.

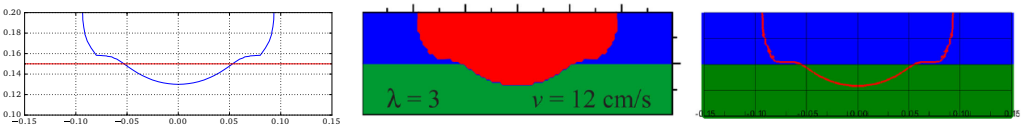

(a) Melt pool depth for $v = 120\frac{\text{mm}}{\text{s}}$. From left to right: this work, Gusarov *et al.* and Hodge *et al.*

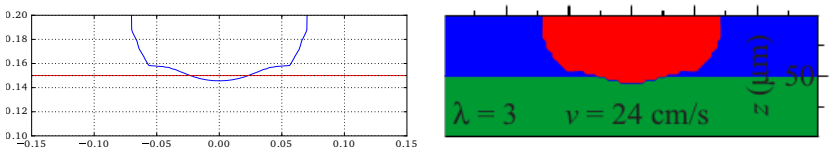

(b) Melt pool depth for $v = 240\frac{\text{mm}}{\text{s}}$. From left to right: this work and Gusarov *et al.*

Figure 7: Melt pool depth for heat source velocities of $v = 120\frac{\text{mm}}{\text{s}}$ and $v = 240\frac{\text{mm}}{\text{s}}$. The cross-sections were taken at maximum melt pool depth.

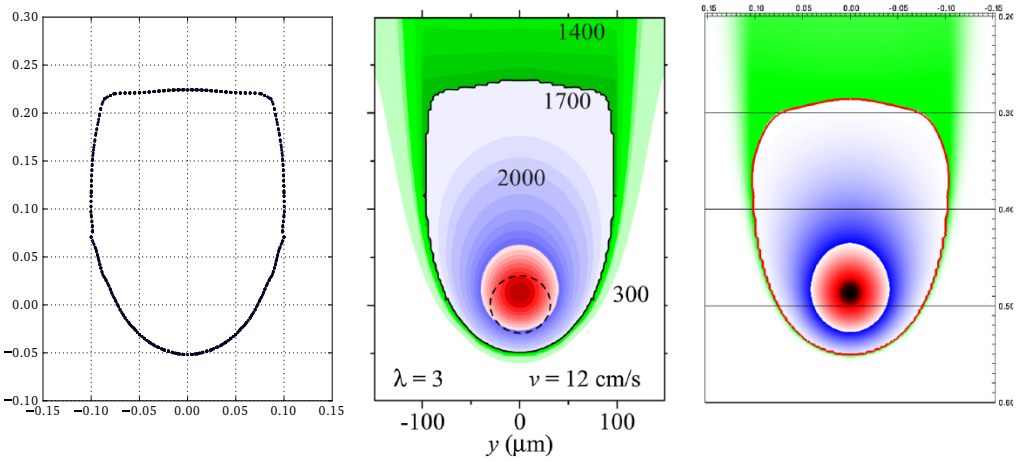

(a) Melt pool shape for $v = 120\frac{\text{mm}}{\text{s}}$. From left to right: this work, Gusarov *et al.* and Hodge *et al.*

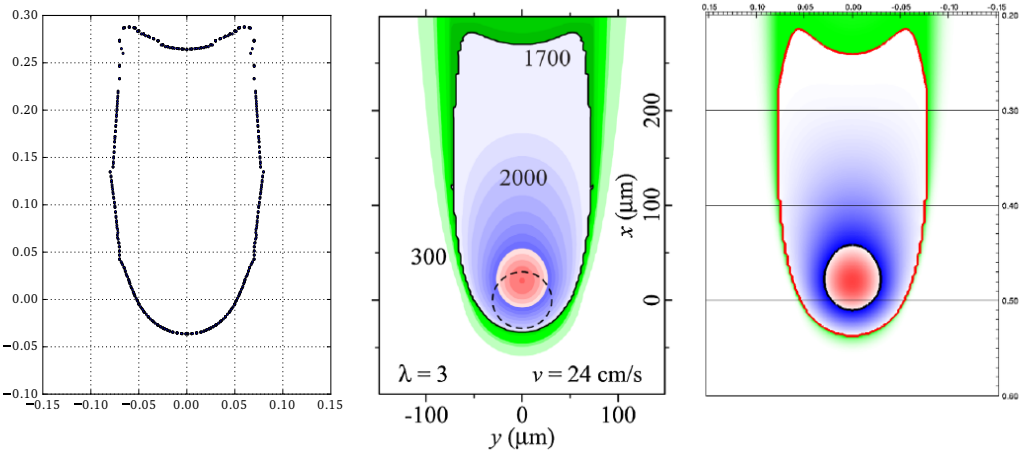

(b) Melt pool shape for $v = 240\frac{\text{mm}}{\text{s}}$. From left to right: this work, Gusarov *et al.* and Hodge *et al.*

Figure 8: Melt pool shape for heat source velocities of $v = 120\frac{\text{mm}}{\text{s}}$ and $v = 240\frac{\text{mm}}{\text{s}}$.

4.2 Example 2: numerical performance of the proposed HROM

The numerical performance of the proposed HROM for the non-linear phase change problem is investigated by studying the $v = 120\frac{\text{mm}}{\text{s}}$ example.The on-line performance of the HROM is tested by running the same problem used for training, with the purpose of showing the stability properties of the HROM.

The HROM proposed in Section 3.1 was used. The snapshots for the reduced generalised forces, Eq. (33), were collected in a *consistent* manner. That is, first the HF model was solved for collecting snapshots of the temperature field. Then, the POD modes $\boldsymbol{\Psi}$ for the temperature field were computed and used for performing the first reduction. Next, the snapshots for the reduced forces were collected by solving the training problem with the ROM resulting from the first reduction. This ensures that the snapshots collection strategy for the reduced forces is consistent. A total of $n_p = 24$ POD modes for the temperature field were used. Every computed time step from the HF model is used as snapshot for the temperature field. No partitioned SVD is used for the computation of the SVD for these POD modes. On the other hand, for the computation of the basis $\boldsymbol{\Phi}$ of the Null space of $\boldsymbol{\mathcal{T}}$, the partitioned SVD algorithm presented in Section 3.3 was used with 9 partitions.

It can be observed from Eq. (22) that a total of five non-linear generalised forces need to be separately hyper-reduced. Therefore, we need to compute five different basis $\boldsymbol{\Phi}$, one for each term, and then to apply the NNLS algorithm in order to select the elements to sample and their corresponding weights. In order to study the convergence of the error obtained with the proposed HROM, an increasing number of selected elements for each non-linear term was tested as specified in Table 2. Due to the fact that the maximum number of elements to be sampled is 700, the partitioned SVD of rank 832 was computed for every term, *i.e.*, twice the number of time steps computed for the HF model.

Non-linear term	Test 1	Test 2	Test 3	Test 4	Test 5	Test 6	Test 7
$\tilde{\boldsymbol{G}}^c$	40	60	80	100	300	500	700
$\tilde{\boldsymbol{G}}^k$	40	60	80	100	300	500	700
$\tilde{\boldsymbol{G}}^{vc}$	40	60	80	100	300	500	700
$\tilde{\boldsymbol{G}}^l$	24	36	48	60	170	290	400
$\tilde{\boldsymbol{G}}^{vl}$	24	36	48	60	170	290	400

Table 2: Number of selected elements to be tested for each non-linear term.

The Frobenius norm of the relative error obtained for each test is given in Fig. 9. We observe from this figure that the proposed HROM behaves well from the stability point-of-view, based on the fact that the error decreases monotonically as the number of sampled elements is increased.

The CPU-times and speedup obtained for the different HROM tests can be observed in Figs. 10a-b. The reference time is the time taken by the HF model running in parallel with 12 threads. The HROM tests were also run in parallel using 12 threads. The time spent writing the solution to disk is part of the time measured for the HF model. The time necessary for writing the solution was also included in the HROM tests. However, in the latter case the solution is written in its reduced form, that is, the generalised DOFs associated to the basis $\boldsymbol{\Psi}$ for the temperature are written. It should be observed that the obtained speedups are not so high if one takes into account that the largest number of sampled elements is 700. This is because the projection of the temperature field from the local to the global domain is not

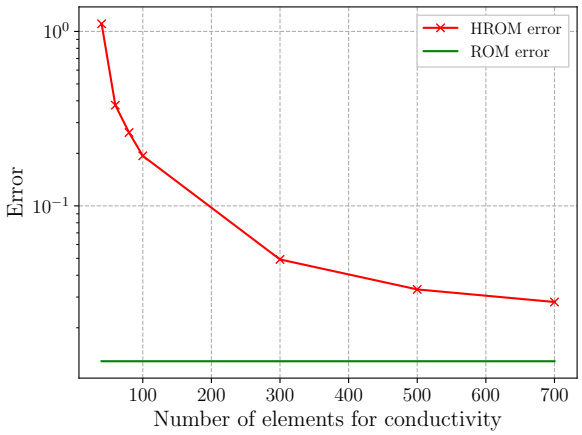

Figure 9: Relative error obtained for each test computed in the Frobenius norm. In the best case, the error obtained for the HROM is 2.8%, whilst the error with ROM is 1.28%.

reduced. Therefore, the expected speedup will be bounded by the time taken by this projection which can be considered as part of the sequential portion of the algorithm. Reducing the time taken by the projection of the temperature field from the local to the global domain will be subject of future work.

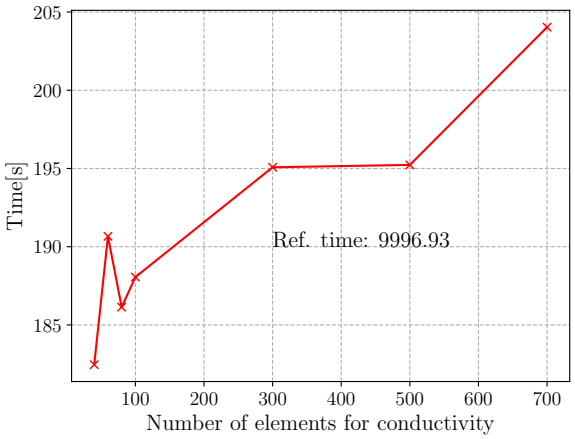

(a) Times for the different HROM tests. The reference time is the time taken by the HF model.

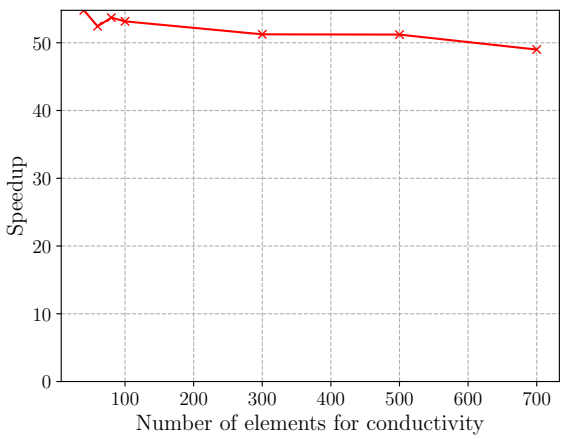

(b) Speedup for the different HROM tests.

Figure 10: Times and speedup obtained for the different HROM tests.

In order to assess the quality of the solution obtained with the HROM model with the parameters of Test 7, the obtained profiles for the melt pool shape and depth and the temperature field are shown in Figs. 11a-c. As it can be seen, the temperature field is well approximated as well as the melt pool depth. However, we cannot say the same for the melt pool shape, which is well approximated by the HROM on the front but not on the back. Nonetheless, it should be observed that in the area corresponding to the back of the melt pool, the temperature field is almost constant. Therefore, small errors in the temperature field computed by the HROM will lead to large differences in the captured shape of the melt pool. However, these errors do not influence the quality of the solution obtained with the HROM from a qualitative point-of-view

as it can be recognised from the results shown in Figs. 12a-f.

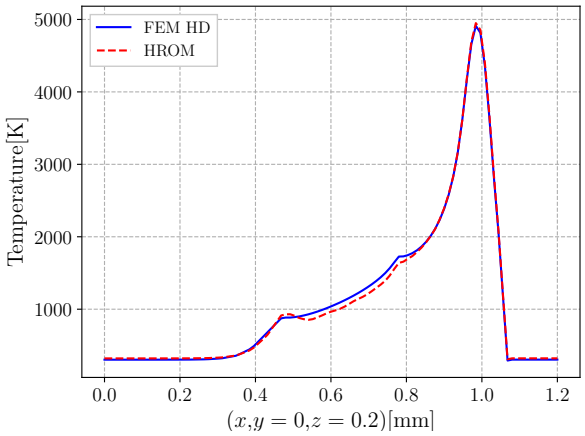

(a) Temperature field along the line $(x, y = 0, z = 0.2)$.

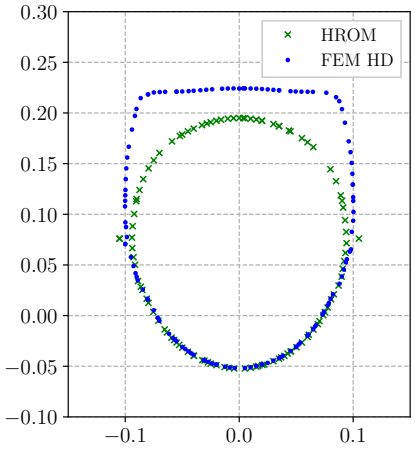

(b) Melt pool shape.

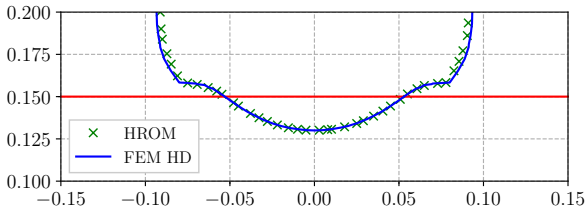

(c) Maximum melt pool depth.

Figure 11: Comparison between the HROM and the HF models at the time instant 0.00416s of the obtained profiles for the melt pool shape and depth and the temperature field. The results for the HROM model correspond to those obtained for Test 7.

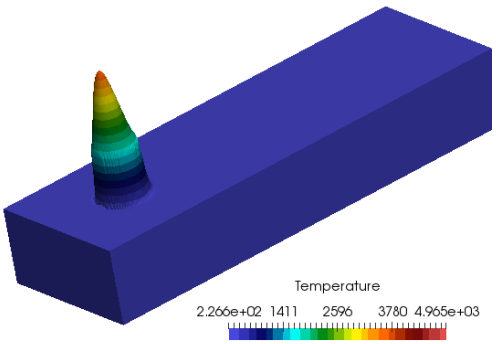

(a) FEM HD 0.0002s

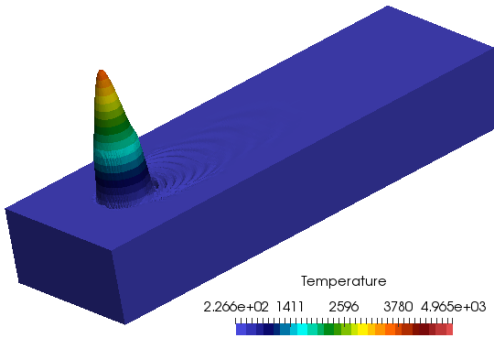

(b) HROM 0.0002s

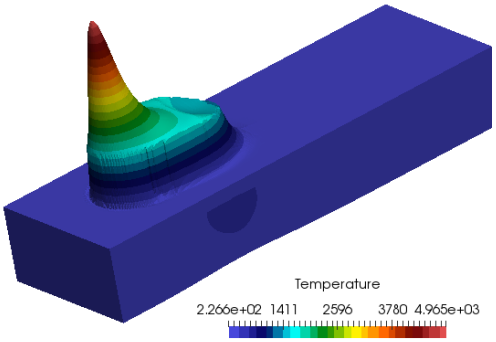

(c) FEM HD 0.0022s

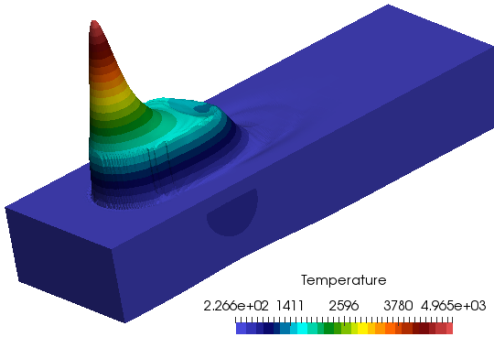

(d) HROM 0.0022s

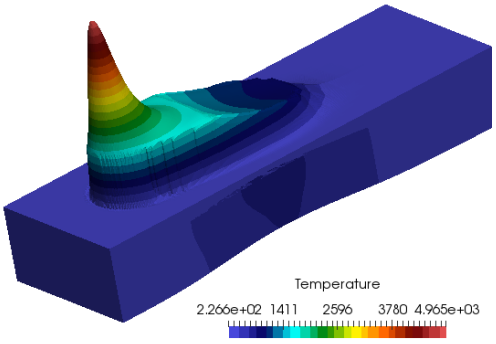

(e) FEM HD 0.00416s

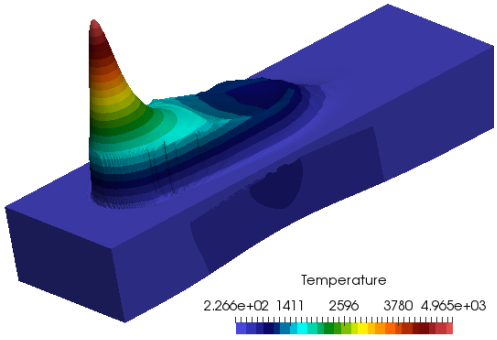

(f) HROM 0.00416s

Figure 12: Temperature field for the local domain at different time instants for the HF model and the HROM with the parameters of Test 7.

5 Conclusions and future work

A *material* Global-Local model for describing the evolution of material phase changes of non-linear problems characterised by highly concentrated moving sources was proposed. This model was successfully applied to the simulation of a Selective Laser Melting Additive Manufacturing problem. The obtained results were comparable to those found in the literature. Following, in order to tackle the computational cost of solving the non-linear thermal phase change problem of the local domain, a HROM based on a variant of the ECSW method was introduced. The behaviour of the HROM was studied by solving a SLM problem, where the on-line performance was tested for the same problem used for training. It was observed that the developed HROM is stable from the point-of-view that as the number of sampled elements is increased, the error decreases. The obtained results approximated the temperature field with a 2.8% of error in the Frobenius norm. The melt pool depth was also well approximated. However, the back of the melt pool shape differed from the one obtained with the HF model. This was attributed to the fact that the temperature field is almost tangent in that area, translating the small error in the temperature field in a large difference in the melt pool shape.

On one hand, future work needs to be done on the high fidelity Global-Local model. In this work in order to study the material coupling between the global and local domains, it was assumed that the temperature field was the solution to a non-linear phase change problem defined only on the local moving domain. The material Global-Local proposed here needs to be extended to the Global-Local model presented in [6] where linear problems are handled but where the coupling of the temperature field between the global and local domains is considered. Another topic is the development of a stabilisation technique specifically conceived for SLM problems.

On the other hand, issues concerning the HROM are subject of future study. One of those issues is the development of good snapshots collection strategies which lead to good on-line behaviour for problems different from those used in the training phase. Another important matter is to study the reduction of the projection of the temperature field from the local to the global domain in order to enable to obtain higher speedups.

References

[1] Idelsohn, S., Storti, M., and Crivelli, L., 1994. "Numerical methods in phase-change problems". pp. 49–74.

[2] Fachinotti, V. D., Cardona, A., and Huespe, A. E., 1999. "A fast convergent and accurate temperature model for phase-change heat conduction". *International Journal for Numerical Methods in Engineering,* **44**(12), pp. 1863–1884.

[3] Goldak, J., and Akhalaghi, M., 2005. *Computational Welding Mechanics*. Springer.

[4] Gusarov, A. V., Yadroitsev, I., Bertrand, P., and Smurov, I., 2009. "Model of radiation and heat transfer in laser-powder interaction zone at selective laser melting". *Journal of Heat Transfer,* **131**(7), p. 072101.

[5] Hodge, N. E., Ferencz, R. M., and Solberg, J. M., 2014. "Implementation of a thermomechanical model for the simulation of selective laser melting". *Computational Mechanics,* **54**(1), apr, pp. 33–51.

[6] Cosimo, A., Cardona, A., and Idelsohn, S., 2017. "Global-Local ROM for the solution of parabolic problems with highly concentrated moving sources". *Computer Methods in Applied Mechanics and Engineering,* **326**(Supplement C), pp. 739 – 756.

[7] Cardona, A., and Idelsohn, S., 1986. "Solution of non-linear thermal transient problems by a reduction method". *International Journal for Numerical Methods in Engineering,* **23**(6), pp. 1023–1042.

[8] Baiges, J., Codina, R., and Idelsohn, S., 2013. "Explicit reduced-order models for the stabilized finite element approximation of the incompressible Navier-Stokes equations". *International Journal for Numerical Methods in Fluids,* **72**(12), pp. 1219–1243.

[9] Cosimo, A., Cardona, A., and Idelsohn, S., 2014. "Improving the k-compressibility of hyper reduced order models with moving sources: Applications to welding and phase change problems". *Computer Methods in Applied Mechanics and Engineering,* **274**(0), pp. 237 – 263.

[10] Chaturantabut, S., and Sorensen, D., 2009. "Discrete empirical interpolation for nonlinear model reduction". In Decision and Control, 2009 held jointly with the 2009 28th Chinese Control Conference. CDC/CCC 2009. Proceedings of the 48th IEEE Conference on, pp. 4316–4321.

[11] Hernández, J., Caicedo, M., and Ferrer, A., 2017. "Dimensional hyper-reduction of nonlinear finite element models via empirical cubature". *Computer Methods in Applied Mechanics and Engineering,* **313**, pp. 687 – 722.

[12] Oliver, J., Caicedo, M., Huespe, A. E., Hernández, J. A., and Roubin, E., 2017. "Reduced order modeling strategies for computational multiscale fracture". *Computer Methods in Applied Mechanics and Engineering,* **313**, pp. 560–595.

[13] An, S. S., Kim, T., and James, D. L., 2008. "Optimizing cubature for efficient integration of subspace deformations". *ACM Trans. Graph.,* **27**(5), Dec., pp. 165:1–165:10.

[14] Farhat, C., Avery, P., Chapman, T., and Cortial, J., 2014. "Dimensional reduction of nonlinear finite element dynamic models with finite rotations and energy-based mesh sampling and weighting for computational efficiency". *International Journal for Numerical Methods in Engineering,* **98**(9), jun, pp. 625–662.

[15] Farhat, C., Chapman, T., and Avery, P., 2015. "Structure-preserving, stability, and accuracy properties of the energy-conserving sampling and weighting method for the hyper reduction of nonlinear finite element dynamic models". *International Journal for Numerical Methods in Engineering,* **102**(5), may, pp. 1077–1110.

[16] Felippa, C., Park, K., and Farhat, C., 2001. "Partitioned analysis of coupled mechanical systems". *Computer Methods in Applied Mechanics and Engineering,* **190**(24-25), pp. 3247–3270.

[17] Dureisseix, D., and Bavestrello, H., 2006. "Information transfer between incompatible finite element meshes: Application to coupled thermo-viscoelasticity". *Computer Methods in Applied Mechanics and Engineering,* **195**(44-47), pp. 6523–6541.

[18] Nouy, A., 2010. "A priori model reduction through proper generalized decomposition for solving time-dependent partial differential equations". *Computer Methods in Applied Mechanics and Engineering,* **199**(23-24), pp. 1603 – 1626.

[19] Ryckelynck, D., 2005. "A priori hyperreduction method: an adaptive approach". *Journal of Computational Physics,* **202**(1), pp. 346 – 366.

[20] Sirovich, L., 1987. "Turbulence and the dynamics of coherent structures. I - Coherent structures. II - Symmetries and transformations. III - Dynamics and scaling". *Quarterly of Applied Mathematics,* **45**, Oct., pp. 561–571.

[21] Strang, G., 1993. "The fundamental theorem of linear algebra". *The American Mathematical Monthly,* **100**(9), pp. pp. 848–855.

[22] Cosimo, A., Cardona, A., and Idelsohn, S., 2016. "General treatment of essential boundary conditions in reduced order models for non-linear problems". *Adv. Model. and Simul. in Eng. Sci.,* **3**(1).

[23] Cosimo, A., Fachinotti, V., and Cardona, A., 2012. "An enrichment scheme for solidification problems". *Computational Mechanics*, pp. 1–19.

[24] Lawson, C., and Hanson, R., 1995. *Solving Least Squares Problems.* Society for Industrial and Applied Mathematics.

[25] Voronin, S., and Martinsson, P.-G., 2015. "RSVDPACK: An implementation of randomized algorithms for computing the singular value, interpolative, and CUR decompositions of matrices on multi-core and GPU architectures". *ArXiv e-prints*, Feb.